ARTICLES
PUBLISHED ONLINE: 5 OCTOBER 2015 | DOI: 10.1038/NPHYS3490
nature physics

Transmission of torque at the nanoscale

Ian Williams[1,2,3†], Erdal C. Oğuz[4,5], Thomas Speck[6], Paul Bartlett[2], Hartmut Löwen[5*] and C. Patrick Royall[1,2,3*]

In macroscopic mechanical devices, torque is transmitted through gearwheels and clutches. In the construction of devices at the nanoscale, torque and its transmission through soft materials will be a key component. However, this regime is dominated by thermal fluctuations leading to dissipation. Here we demonstrate the principle of torque transmission for a disc-like colloidal assembly exhibiting clutch-like behaviour, driven by 27 particles in optical traps. These are translated on a circular path to form a rotating boundary that transmits torque to additional particles confined to the interior. We investigate this transmission and find that it is determined by solid-like or fluid-like behaviour of the device and a stick–slip mechanism reminiscent of macroscopic gearwheels slipping. The transmission behaviour is predominantly governed by the rotation rate of the boundary and the density of the confined system. We determine the efficiency of our device and thus optimize conditions to maximize power output.

Classical thermodynamics evolved in response to the need to understand, predict and optimize the steam engines responsible for driving the industrial revolution[1]. In contrast to these macroscopic devices, 'soft' engines at the nanoscale operate in the presence of thermal fluctuations. When the thermal energy is of the same order as the work done, these fluctuations pose a fundamental challenge and call for new design principles. Nanomachines have been studied theoretically[2], particularly in the case of molecular motors[3,4]. Experimentally, colloidal and nanoparticle systems provide insight into fundamental thermodynamic processes in the presence of stochastic Brownian noise[5,6]. Single colloidal particles manipulated by optical forces have been used to, for example, realize the analogue of a Stirling engine[7], to explore the nanoscopic manifestation of the second law of thermodynamics[8,9] and to emulate memory devices testing Landauer's principle for the work dissipated when erasing information[10]. The next stage is to exploit these insights from model systems to engineer devices that perform predictably in the presence of thermal fluctuations.

An important step in this direction would be a microscopic gearbox or transmission system. Although rotational devices have been fabricated[11–13], and nanoscopic gearwheels realized[14,15], such devices are typically single rigid objects driven to rotate by, for example, optical forces[12–14], magnetic forces[16], rectified bacterial motion[15] or asymmetric catalytic activity[17,18]. However, nanoscale devices are frequently engineered using soft components, and the self- or directed assembly of nanometric building blocks into soft mesostructures represents an exciting opportunity for the realization of microscopic machines[19–25]. The response of a soft material to an external force is fundamentally different from that of a rigid body and the transmission of torque through soft materials remains little explored despite its clear importance if nanoscale mechanical devices are to be developed. Because nanoparticle, colloidal and biological systems are typically suspended in a fluid medium, it is natural to investigate the effect of such a medium on a soft rotational device. It is clear from considerations of the effects of inertia in small bodies that the influence of the immersing fluid will be profound[26].

Here we tackle the transmission of torque in soft devices. We realize a driven colloidal assembly exhibiting clutch-like behaviour and identify new mechanisms important to the transmission of torque through soft materials at the nanoscale. Our device is created in a quasi-two-dimensional colloidal system in which $n = 27$ particles are held in a circular configuration of radius R using holographic optical tweezers[27]. The interior region is populated with N identical (but untweezed) particles, creating a circularly confined system, as shown in Fig. 1 (ref. 28). The boundary is rotated to provide torque to the assembly. Details are provided in the Methods. The speed of this rotation is characterized by the Péclet number, Pe, defined in the Methods, with a larger Pe indicating faster rotation.

To understand the key aspects of the dynamical behaviour, we perform Brownian dynamics simulations with parameters matched to the experiments. In the experiments, the driven boundary exerts forces on the solvent, creating a fluid velocity field affecting the motion of the confined population. In simulation we determine an effective solvent flow field by superposing the flow fields due to each of the $n = 27$ driven particles. Full simulation details are provided in the Methods.

Altering the radius of the driven boundary *in situ* allows torque transmission to be engaged or disengaged at will, forming a minimal model of a 'nanoclutch'. We investigate different regimes of torque transmission to the centre of the assembly dependent on Péclet number and the density of the confined population. Owing to the softness of the colloidal system, under certain conditions the rotational behaviour is markedly different from that of a rigid body. We consider the consequences of this for the efficiency of such systems. Our analysis reveals periodic structural self-similarity of geometric origin, related to slip between particle layers, leading to clutch-like behaviour due to a decoupling between driven and loaded parts of the device.

[1]H. H. Wills Physics Laboratory, Tyndall Avenue, Bristol BS8 1TL, UK. [2]School of Chemistry, Cantock's Close, University of Bristol, Bristol BS8 1TS, UK. [3]Centre for Nanoscience and Quantum Information, Tyndall Avenue, Bristol BS8 1FD, UK. [4]Department of Chemistry, Princeton University, Princeton, New Jersey 08544, USA. [5]Institut für Theoretische Physik II, Heinrich-Heine-Universität, D-40225 Düsseldorf, Germany. [6]Institut für Physik, Johannes Gutenberg-Universität Mainz, Staudingerweg 7-9, D-55128 Mainz, Germany. †Present address: Department of Chemical Engineering, University of California Santa Barbara, Santa Barbara, California 93106, USA. *e-mail: hlowen@hhu.de; paddy.royall@bristol.ac.uk

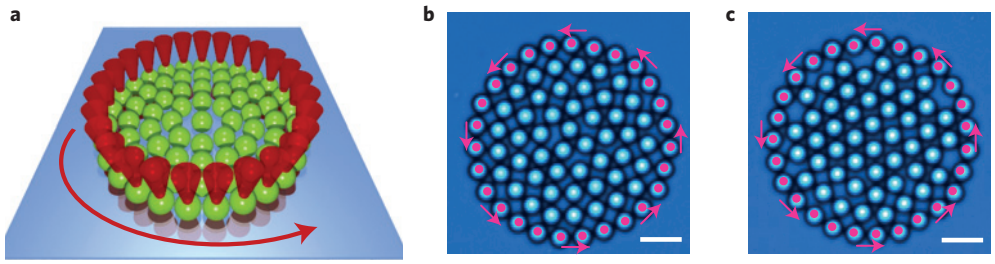

Figure 1 | The experimental system. a, Schematic of a model nanoclutch. Red cones represent optical traps translating 27 particles on a circular path. **b**,**c**, The interior is populated with $N=48$ particles and assumes a bistable state, either layered fluid, $\psi_6 \lesssim 0.8$ (**b**) or locally hexagonal, $\psi_6 \gtrsim 0.8$ (**c**). Particles marked with magenta dots are optically trapped and translated in the direction indicated by the arrows. Scale bars, 10 μm.

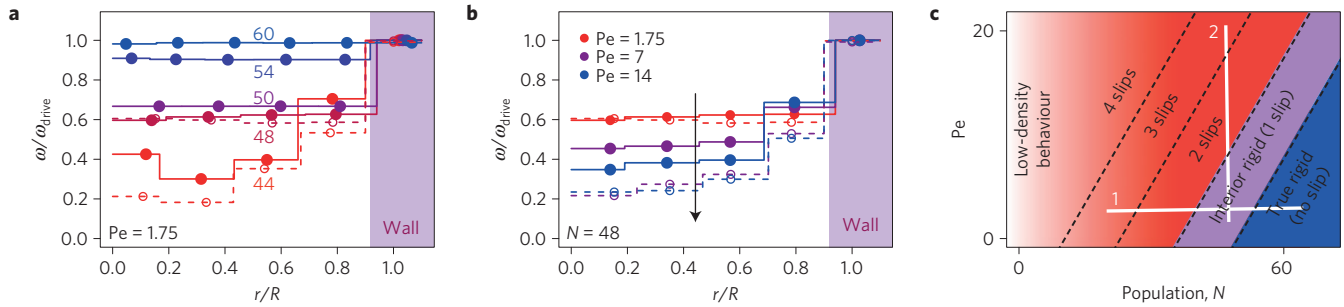

Figure 2 | Controlling rotational behaviour with *N* and Pe. a, Normalized angular velocity profiles for varying N measured in simulation (filled circles and solid lines) and experiment (open circles and dashed lines) at Pe = 1.75. Labels indicate N. Purple region is the boundary. **b**, Normalized angular velocity profiles for varying Pe measured in simulation (filled circles and solid lines) and experiment (open circles and dashed lines) at $N=48$. Arrow indicates direction of increasing Pe. Purple region is the boundary. **c**, Schematic non-equilibrium state diagram showing behaviour in terms of the number of slips as a function of N and Pe. White lines indicate position of data series shown in **a**, 1, and **b**, 2.

Rotational behaviour

Soft materials, such as assemblies of colloids, are much more susceptible to external perturbation (in the case of shear) than macroscopic solid bodies. This opens the possibility to exploit the mechanical properties of the material to modify the transmission itself. We first consider the system in its quiescent state. At sufficient density ($N \geq 47$), the static system exhibits a bistability between locally hexagonal and layered fluid configurations, as shown in Fig. 1b,c (refs 28,29). Hexagonality is quantified using the average bond-orientational order parameter ψ_6 (defined in the Methods). Without boundary rotation, both hexagonal and layered configurations are solid on the experimental timescale—the structural relaxation time exceeds the experimental duration.

On rotation, we observe multiple modes of transmission, dependent on both the confined population and Péclet number Pe, identified by qualitatively distinct angular velocity profiles. Figure 2a shows the effect of varying N at Pe = 1.75, where the angular velocity is averaged within particle layers and plotted with a point at the layer centre of mass. For $N=44$ (red data) the angular velocity profile has a step-like form, with sharp discontinuous changes indicating slipping between circular layers rotating with different angular velocities. Here, in both simulation (solid red line) and experiment (dashed red line) one can clearly identify three slip locations between layers. On increasing the interior population to $N=48$ (red-purple lines) only a single slip is observed, occurring at $r/R \approx 0.9$, between the driven boundary and the confined population. Inside the wall the angular velocity profile is flat, indicating rigid-body-like rotation of the interior. Such interior-rigid behaviour persists in simulations of populations up to $N=54$, albeit with the degree of slip decreasing on increasing N. By $N=60$ (blue line) there is no longer any slip between the boundary and the interior, resulting in a flat angular velocity profile at $\omega(r)=\omega_{\mathrm{drive}}$, characteristic of full rigid body rotation. Note that at the greatest populations studied in simulation ($N=54$ and $N=60$) a structural rearrangement must occur, resulting in the formation of a fifth particle layer and an outwards displacement of the wall particles.

Holding the population constant at $N=48$ and increasing Pe also results in the development of slip rings. This is illustrated in Fig. 2b. At Pe = 1.75 both experiment (open red data) and simulation (solid red data) exhibit interior-rigid rotation, characterized by a flat angular velocity profile at $\omega \approx 0.6\,\omega_{\mathrm{drive}}$ in the interior of the device. By Pe = 7 a second slip has developed in both experiment and simulation.

Figure 2c shows the non-equilibrium state diagram in terms of N and Pe. Rotational behaviour is characterized by the number of slip rings. Taking an initially rigid system and either increasing the driving speed or decreasing the population results in the sequential development of slip rings. This starts with the boundary slipping over the interior (interior rigid) and propagates inwards. Slips develop between adjacent particle layers; thus, their radial location is determined by the structure of the confined assembly. When altering N, small changes in slip locations are observed as the layered structure shifts to larger r at higher density. At constant population, the radial slip locations remain unchanged as Pe is increased.

The line labelled '1' in Fig. 2c represents the approximate location of the constant Pe data series presented in Fig. 2a, whereas '2' represents the constant N series shown in Fig. 2b. Video examples of multiple slip and interior-rigid behaviours from experiments with $N=48$ are available as Supplementary Movies 1 (multiple slip) and 2 (interior rigid). Simulated data showing full rigid body rotation can be seen in Supplementary Movie 3.

Exploiting the dependence of rotational behaviour on N allows clutch-like operation by altering the internal density *in situ*. Figure 3 illustrates this in a single simulation at $N=48$, in which the radial location of the boundary is increased during the simulation, reducing the internal density. On increasing this radius from $R_{\mathrm{sim}}=0.969R$ to $R_{\mathrm{sim}}=1.046R$, slips develop between layers. Thus we demonstrate that not only does the rotational behaviour depend on

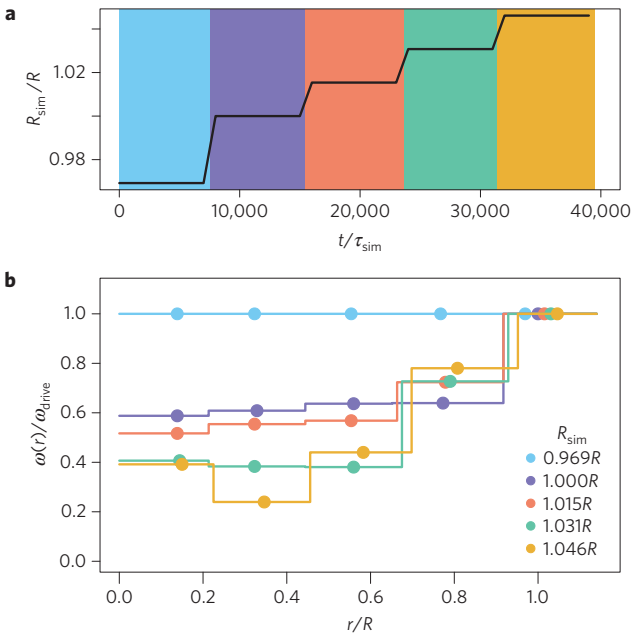

Figure 3 | Disengaging transmission *in situ* by altering density in a single simulation with $N=48$. a, Radial location of boundary as a function of time in simulation time units. R is the radius of the experimental system and R_{sim} is the simulated radius, given in terms of R. **b**, Angular velocity profiles in the five simulated time intervals indicated by the colour shading in **a**.

the internal population, but that this effect can be employed as an active control mechanism, engaging or disengaging a microscopic rotational device at will in a clutch-like operation mode. In Supplementary Fig. 1 and Supplementary Note I, we show that *in situ* alteration of Pe allows similar control of rotational behaviour. Thus, clutch-mode operation can be realized through variations in both driving speed and internal density, or combinations thereof, effectively 'dialling in' the desired behaviour.

Although we focus on the system with a boundary of $n=27$ particles, resulting in a confined assembly of four particle layers for all but the largest populations, simulations are also performed for smaller, $n=21$, and larger, $n=33$ boundaries, with three and five layers respectively. Angular velocity profiles measured in these systems, analogous to those in Fig. 2a,b, are shown in Supplementary Fig. 2 and described in Supplementary Note II. In both these systems the same phenomena are observed with the same dependence on N and Pe, indicating that the mechanisms revealed here are not specific to the four-layer device geometry.

That the slip behaviour depends on controllable parameters is a striking difference between this softly coupled rotational system and the rigid rotational elements investigated previously[12–16]. Here we can control not only the speed with which the device rotates, but also the manner in which this rotation is transmitted through the system. With the development of each successive slip ring, the angular velocity at the centre of the system is reduced relative to that imposed at the boundary, and thus the torque transmission is modified and, one would expect, rendered less efficient. In other words, one may say that such soft materials exhibit 'self-lubrication'.

Efficiency

Having described the rotational behaviour we now consider its efficiency for torque transmission. By controlling the slip behaviour we can tune the transmission of torque from the boundary to the centre. Work is spent through the rotation of the boundary, much of which is dissipated into the surrounding solvent. Nevertheless, because the externally applied torque is transmitted to the innermost particles, useful work can be extracted by attaching an axle, which may be manufactured using commercially available laser lithography nanofabrication techniques[30,31]. A schematic of this is shown in Fig. 4a.

If an external load applies a constant torque, τ, to the axle, the extracted power is $P_o=\tau\,\omega(\tau)$. Here $\omega(\tau)$ is the angular velocity of the loaded axle. We define the isothermal efficiency as the ratio $\eta=P_o/P_i$ of extracted power to input power P_i—that is, the work spent per unit time[3,32]. The latter can be expressed as $P_i=n\,\omega_{drive}\,\tau_{drive}$ with $n=27$ (the number of optically trapped particles), where τ_{drive} is the driving torque applied to each of the trapped particles. This definition of efficiency is not unique, but is appropriate here as it relates the mechanical work necessary to move the outer particles to the torque generated at the centre of the device.

This situation is realized in simulation by applying a constant torque to the central particles in the opposite direction to the imposed boundary rotation. The points in Fig. 4e show the efficiency obtained from simulations at $N=48$ as a function of the torque ratio for $Pe=1.75$ (blue) and $Pe=7$ (red). Efficiency is maximized at an optimal load torque. Further loading reduces the efficiency until the device stalls and the extracted power is zero. Here there is, on average, no rotation of the central particles, and the softness of the assembly allows the outer particles to slip. Beyond the stall torque, the central particles rotate in the opposite direction to the driven particles as the loading dominates the driving. These behaviours are illustrated in Fig. 4b–d and Supplementary Movies 4 (transmission), 5 (stall) and 6 (slip dominated). At $Pe=1.75$ (blue data) the system exhibits interior-rigid rotation whereas at $Pe=7$ (red data) two slip rings exist. This qualitative change in the angular velocity profile manifests as a relative reduction in the efficiency of torque transmission from the boundary to the system centre.

In the experiments, there is no axle—hence $\tau=0$ and all the input power is dissipated. However, from the measured angular velocities in the innermost particle layer, ω, we can determine the efficiency in the linear response regime for small τ, which provides an upper bound $\eta\leq n^{-1}(\omega(\tau=0)/\omega_{drive})(\tau/\tau_{drive})$. Here τ_{drive} is calculated from the average angular lag of wall particles behind their optical traps, θ, as $\tau_{drive}=kR^2\langle\sin\theta\rangle$. The derivation of these quantities is presented in the Methods. The gradient of this experimentally measured upper bound on η is shown as a function of Pe for $N=48$ in Fig. 4f, and the inset shows $\langle\sin\theta\rangle$, which increases linearly with Pe. The dashed lines in Fig. 4e are these upper bounds for the two simulated Péclet numbers. As demonstrated in the inset, we find excellent agreement with the simulation data at small τ. Although the measured efficiencies are small, it should be noted that efficiencies of a comparable order of magnitude are common in micro- and nanoscale systems, in which thermal fluctuations are important. For instance, swimming efficiencies of $\sim10^{-5}$ are reported for a model self-propelled diffusiophoretic particle[33].

Mechanism of transmission control

Our particle-resolved experiments allow us to pinpoint the transmission control mechanism. In the rigid and interior-rigid regimes, local structure in the confined assembly is maintained during rotation. However, when layers slip past one another, the local environment around a given particle is in constant flux as its nearest neighbours change. Restricting attention to a single experiment with $N=48$ driven at $Pe=19.25$, variations in local structure can be seen in the behaviour of average ψ_6 with time within each of four particle layers. These are shown in Fig. 5a–d, where the orange, green, blue and red lines correspond to the highlighted layers in Fig. 5e. Time is scaled by the rotation period, t_{rot}. In all but the central region, ψ_6 explores a large range, indicating that the local structure is alternately driven between highly hexagonal and disordered arrangements—rotating the boundary drives the internal structure between the two bistable configurations observed in the

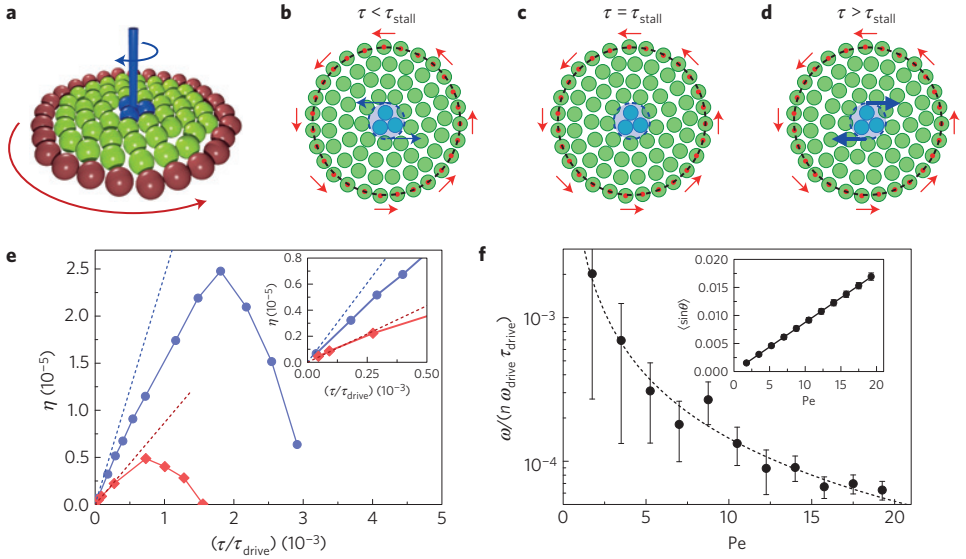

Figure 4 | Measuring efficiency in the loaded device. a, System schematic with an axle attached to the central three particles (blue). Red particles are the boundary. **b**–**d**, Three behaviours when the device works against an external load torque, τ. The boundary is driven in the direction of the red arrows. The central three particles rotate in the direction of the blue arrows. **e**, Efficiency as a function of torque ratio as measured in simulation for Pe = 1.75 (blue) and Pe = 7 (red). Dashed lines are the experimentally measured upper bounds on efficiency in the linear response regime. Inset shows efficiency in the low torque limit. Error bars are smaller than the symbols. **f**, Experimentally measured gradient of the upper bound on efficiency in the linear response regime as a function of Pe. Dashed line is a guide to the eye. Error bars are calculated from the relative error, given by $[(\Delta k/k)^2 + 2(\Delta R/R)^2 + (\Delta(\omega/\omega_{\mathrm{drive}})/(\omega/\omega_{\mathrm{drive}}))^2 + (\Delta(\langle\sin\theta\rangle)/\langle\sin\theta\rangle)^2]^{1/2}$, where the uncertainties Δk and ΔR result from the parabolic fitting to the optical trap potential, $\Delta(\omega/\omega_{\mathrm{drive}})$ is the standard deviation in the relative angular velocity measured at the centre and $\Delta(\langle\sin\theta\rangle)$ is the standard deviation in sine of the measured lag angle. Inset shows the measured angular lag of wall particles behind their optical traps.

quiescent system[28,29]. Furthermore, in all but the central region, this occurs with some characteristic frequency—fastest in the wall-adjacent layer, and more slowly in the third and second layers.

By considering the time autocorrelation of fluctuations in ψ_6 about its mean, the periodicity in ψ_6 in each layer is extracted. Figure 5 shows these autocorrelation functions for all slipping data with population $N = 48$ in layer 3 (f) and layer 4 (g)—the blue and red regions shown in e. When time is scaled by t_{rot}, a common first peak develops in these functions for all samples exhibiting at least two slips, indicating a common period for fluctuations in ψ_6 at timescale of $\sim 0.08 t_{\mathrm{rot}}$ in layer 4 and $\sim 0.23 t_{\mathrm{rot}}$ in layer 3. No such common peak is observed in layers 2 or 1—and as such the data are not shown. These timescales are interpreted as those of structural self-similarity within these two layers. For the range of rotation speeds explored these timescales are independent of Pe when time is rescaled by t_{rot} and are identified as the time taken for a given particle to be overtaken by its faster-moving neighbour in the outer adjacent layer.

Consider the angular velocity of layer 4, $\omega_4 \approx 0.5\omega_{\mathrm{drive}}$ (see Fig. 2b). In the laboratory frame, the angular velocity of the wall is defined as $\omega_{\mathrm{drive}} = 2\pi$ radians per t_{rot}. In a reference frame that co-rotates with layer 4, however, the wall moves with angular velocity $\omega^{(4)}_{\mathrm{wall}} = \omega_{\mathrm{drive}} - 0.5\omega_{\mathrm{drive}} = 0.5\omega_{\mathrm{drive}} = \pi$ radians per t_{rot}. The wall consists of 27 particles, and thus the angular displacement required for a wall particle to move one place around the circumference of the circle is $\delta\phi = 2\pi/27 \approx 0.074\pi$ radians. In the layer 4 co-rotating frame, the time for a wall particle to undergo this angular displacement while moving with constant angular velocity $\omega^{(4)}_{\mathrm{wall}}$ is $\delta\phi/\omega^{(4)}_{\mathrm{wall}} = 0.074 t_{\mathrm{rot}}$. This is remarkably close to the experimentally measured periodicity of $0.08 t_{\mathrm{rot}}$. Performing a similar calculation for the behaviour of layer 3, and noting that layer 4 contains 21 rather than 27 particles, predicts a periodicity of $0.024 t_{\mathrm{rot}}$, which is again very similar to the measured timescale of $0.023 t_{\mathrm{rot}}$. The accuracy of these predictions suggests that, in a given layer, this behaviour is dominated by the faster-moving outer neighbouring layer. Although the layer in question will eventually overtake its slower-moving inner neighbouring layer, this process occurs over a much longer timescale—thus the periodicity depends primarily on the angular velocity of the outer layer. Furthermore, we find no change in this periodicity in simulations with torque applied, suggesting that the extraction of work at the centre does not affect the slip behaviour nearer the boundary.

The overtaking process is illustrated in Fig. 5h, which shows how the local environment around the cyan particle evolves when particle layers slip over one another. This particle initially has six neighbours, drawn in yellow. As rotation proceeds, the outermost layer overtakes its inner neighbouring layer, resulting in a new set of neighbours for the cyan particle. As part of this process the cyan particle briefly has seven neighbours, suppressing its ψ_6. This is ultimately the origin of the fluctuations observed in Fig. 5c,d. Given sufficient time, the cyan particle will overtake its inner neighbour, resulting in its five-fold coordination and again a suppression of ψ_6. In other words, the device exhibits a spatial–temporal periodicity related to layers slipping past one another. This provides a slip mechanism which ultimately leads to stalling and breakdown of transmission when the central particles are sufficiently loaded. Interpreted another way, this mechanism may be thought of as relaxation in shearing a glassy system under strong confinement. The fact we can measure the forces on the tweezed particles may offer ways to directly investigate theories of the glass transition[34].

Discussion

It is possible to exploit the properties of colloidal assemblies to provide a transmission control mechanism reminiscent of a clutch, which is unique to such soft materials. Although here we employed micron-sized colloidal particles, we emphasize that the behaviour we report should remain essentially unaltered provided the constituent particles are large enough such that the solvent can be treated as a continuum—that is, around 10 nm in size. Our investigations underline the need to carefully characterize the behaviour

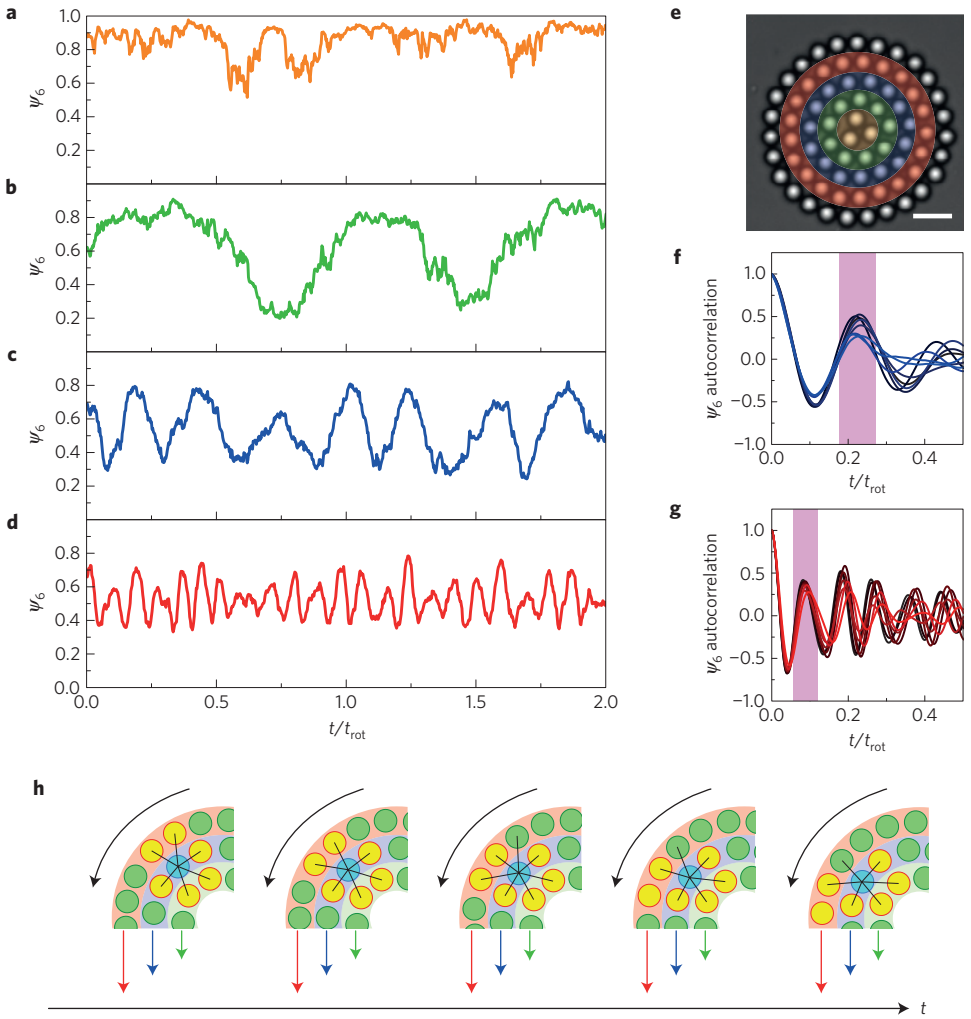

Figure 5 | Structural fluctuations. a–d, Time dependence of ψ_6 in a single experiment at $N=48$ and Pe$=19.25$ resolved within layers indicated by colour in **e**. **a**, Central layer. **b**, Layer 2. **c**, Layer 3. **d**, Layer 4, adjacent to the boundary. **e**, Micrograph indicating the identification of particle layers. Scale bar is, 10 μm. **f**,**g**, ψ_6 autocorrelation for all slipping samples at $N=48$ in layers 3 (**f**) and 4 (**g**). **h**, Illustration of local structural changes caused by the outer layer overtaking the inner layer.

of materials in far-from-equilibrium conditions if they are to be employed in the fabrication of working engines at small length scales.

We expect this kind of controllable transmission from rigid-body (solid-like) to slipping (fluid-like) behaviour to be generic to a range of soft materials with a suitable yield stress, including protein gels, hydrogels and granular matter. Our work represents an important step in the fabrication of mechanical devices, such as gearboxes at the nanoscale, and illustrates the application of soft-matter physics, developed to tackle colloidal systems, to device design. We expect that devices where torque control is essential[35] may come to rely on the controllable transmission mechanisms we present.

Methods

Methods and any associated references are available in the online version of the paper.

Received 11 February 2015; accepted 25 August 2015; published online 5 October 2015

References

1. Carnot, S. *Réflexions sur la puissance motrice du feu et sur les machine propres à développer cette puissance* (Bachelier, 1824).
2. Seifert, U. Efficiency of autonomous soft nanomachines at maximum power. *Phys. Rev. Lett.* **106,** 020601 (2011).
3. Parmeggiani, A., Jülicher, F., Ajdari, A. & Prost, J. Energy transduction of isothermal ratchets: Generic aspects and specific examples close to and far from equilibrium. *Phys. Rev. E* **60,** 2127–2140 (1999).
4. Kolomeisky, A. B. Motor proteins and molecular motors: How to operate machines at the nanoscale. *J. Phys. Condens. Matter* **25,** 463101 (2013).
5. Babič, D., Schmitt, C. & Bechinger, C. Colloids as model systems for problems in statistical physics. *Chaos* **15,** 026114 (2005).
6. Pesce, G., Volpe, G., Imparato, A., Rusciano, G. & Sasso, A. Influence of rotational force fields on the determination of the work done on a driven Brownian particle. *J. Opt.* **13,** 044006 (2011).
7. Blickle, V. & Bechinger, C. Realization of a micrometre-sized stochastic heat engine. *Nature Phys.* **8,** 143–146 (2012).
8. Carberry, D. M. *et al.* Fluctuations and irreversibility: An experimental demonstration of a second-law-like theorem using a colloidal particle held in an optical trap. *Phys. Rev. Lett.* **92,** 140601 (2004).
9. Gieseler, J., Quidant, R., Dellago, C. & Novotny, L. Dynamic relaxation of a levitated nanoparticle from a non-equilibrium steady state. *Nature Nanotech.* **9,** 358–364 (2014).
10. Bérut, A. *et al.* Experimental verification of Landauer's principle linking information and thermodynamics. *Nature* **483,** 187–189 (2012).
11. Klapper, Y., Sinha, N., Ng, W. T. S. & Lubrich, D. A rotational DNA nanomotor driven by an externally controlled electric field. *Small* **6,** 44–47 (2010).
12. Asavei, T. *et al.* Optically trapped and driven paddle-wheel. *New J. Phys.* **15,** 063016 (2013).
13. Lin, X.-F. *et al.* A light-driven turbine-like micro-rotor and study on its light-to-mechanical power conversion efficiency. *Appl. Phys. Lett.* **101,** 113901 (2012).

14. Galajda, P. & Ormos, P. Complex micromachines produced and driven by light. *Appl. Phys. Lett.* **78,** 249–251 (2001).
15. Di Leonardo, R. *et al.* Bacterial ratchet motors. *Proc. Natl Acad. Sci. USA* **107,** 9541–9545 (2010).
16. Xia, H. *et al.* Ferrofluids for fabrication of remotely controllable micro-nanomachines by two-photon polymerization. *Adv. Mater.* **22,** 3204–3207 (2010).
17. Fournier-Bidoz, S., Arsenault, A. C., Manners, I. & Ozin, G. A. Synthetic self-propelled nanorotors. *Chem. Commun.* **2005,** 441–443 (2005).
18. Gibbs, J. G. & Zhao, Y.-P. Design and characterization of rotational multicomponent catalytic nanomotors. *Small* **5,** 2304–2308 (2009).
19. Whitesides, G. M. & Boncheva, M. Beyond molecules: Self-assembly of mesoscopic and macroscopic components. *Proc. Natl Acad. Sci. USA* **99,** 4769–4774 (2002).
20. Kim, Y., Shah, A. A. & Solomon, M. J. Spatially and temporally reconfigurable assembly of colloid crystals. *Nature Commun.* **5,** 3676 (2014).
21. Puigmartí-Luis, J., Saletra, W. J., González, A., Amabilino, D. B. & Pérez-García, L. Bottom-up assembly of a surface-anchored supramolecular rotor enabled using a mixed self-assembled monolayer and pre-complexed components. *Chem. Commun.* **50,** 82–84 (2014).
22. Ismagilov, R. F., Schwartz, A., Bowden, N. & Whitesides, G. M. Autonomous movement and self-assembly. *Angew. Chem. Int. Ed.* **41,** 652–654 (2002).
23. Grzelczak, M., Vermant, J., Furst, E. M. & Liz-Marzán, L. M. Directed self-assembly of nanoparticles. *ACS Nano* **4,** 3591–3605 (2010).
24. Kraft, D. J. *et al.* Surface roughness directed self-assembly of patchy particles into colloidal micelles. *Proc. Natl Acad. Sci. USA* **109,** 10787–10792 (2012).
25. Sacanna, S., Irvine, W. T. M., Chaikin, P. M. & Pine, D. J. Lock and key colloids. *Nature* **464,** 575–578 (2010).
26. Purcell, E. M. Life at low reynolds number. *Am. J. Phys.* **45,** 3–11 (1977).
27. Bowman, R. W. & Padgett, M. J. Optical trapping and binding. *Rep. Prog. Phys.* **76,** 026401 (2013).
28. Williams, I. *et al.* The effect of boundary adaptivity on hexagonal ordering and bistability in circularly confined quasi hard discs. *J. Chem. Phys.* **140,** 104907 (2014).
29. Williams, I., Oğuz, E. C., Bartlett, P., Löwen, H. & Royall, C. P. Direct measurement of osmotic pressure via adaptive confinement of quasi hard disc colloids. *Nature Commun.* **4,** 3555 (2013).
30. Phillips, D. B. *et al.* An optically actuated surface scanning probe. *Opt. Express* **20,** 29679–29693 (2012).
31. Phillips, D. B. *et al.* Force sensing with a shaped dielectric micro-tool. *Europhys. Lett.* **99,** 58004 (2012).
32. Seifert, U. Stochastic thermodynamics, fluctuation theorems and molecular machines. *Rep. Prog. Phys.* **75,** 126001 (2012).
33. Sabass, B. & Seifert, U. Dynamics and efficiency of a self-propelled, diffusiophoretic swimmer. *J. Chem. Phys.* **136,** 064508 (2012).
34. Yoshino, H. Replica theory of the rigidity of structural glasses. *J. Chem. Phys.* **136,** 214108 (2012).
35. Yim, M. *et al.* Modular self-reconfigurable robot systems. *IEEE Robot. Autom. Mag.* **14,** 43–52 (2007).

Acknowledgements

We acknowledge J. Eggers, M. Heinen and R. Jack for helpful discussions. C.P.R. and I.W. acknowledge the Royal Society and European Research Council (ERC Consolidator Grant NANOPRS, project number 617266). Additionally, I.W. was supported by the Engineering and Physical Sciences Research Council (EPSRC). The work of E.C.O. and H.L. was supported by the ERC Advanced Grant INTERCOCOS (project number 267499). E.C.O. was also supported by the German Research Foundation (DFG) within the Postdoctoral Research Fellowship Program (project number OG 98/1-1).

Author contributions

I.W. and C.P.R. conceived the experiments. I.W. built the experimental apparatus and performed the experiments. E.C.O., C.P.R. and H.L. conceived the simulations. E.C.O. carried out the simulations. T.S. performed the theoretical efficiency analysis. All authors contributed to the data analysis and writing of the manuscript.

Additional information

Supplementary information is available in the online version of the paper. Reprints and permissions information is available online at www.nature.com/reprints. Correspondence and requests for materials should be addressed to H.L. or C.P.R.

Competing financial interests

The authors declare no competing financial interests.

Methods

Experimental details. We employ a quasi-two-dimensional colloidal sample of polystyrene spheres of diameter $\sigma = 5\,\mu m$ and polydispersity $s = 2\%$ suspended in a water–ethanol mixture at a mass ratio of 3:1. Under these conditions the particles are slightly charged and interact via a screened electrostatic repulsion with Debye length $\lambda_D \approx 25\,nm$. The gravitational length of these particles is $l_g/\sigma = 0.015 \pm 0.001$, resulting in gravitational confinement to a monolayer adjacent to the glass coverslip substrate in an inverted microscope. This coverslip is treated with Gelest Glassclad 18 to prevent particle adhesion.

Twenty-seven particles are manipulated using holographic optical tweezers[27]. These traps are well-approximated by parabolae with spring constant $k = 420(5)\, k_B T \sigma^{-2}$, extracted by observing the constrained Brownian motion of particles in optical traps[29]. Timescales are set by the Brownian diffusion time, empirically determined as $\tau_B \approx 70.2\,s$. Particle trajectories are extracted[36] for $N = 48$ and $N = 44$, corresponding to effective area fractions $\phi \approx 0.74$ and $\phi \approx 0.79$, respectively.

The boundary is rotated by translating the array of optical traps around a circular path in discrete steps of length $\sigma/8$. Rotation speed is defined by the frequency of these steps, and is characterized by the Péclet number, which is the ratio of the Brownian diffusion time to the time taken to drive a boundary particle a distance σ along its circular path. We report data for Péclet numbers in the range $1.75 \le Pe \le 19.25$, corresponding to optical trap step rates between 0.1 and $1.1\,s^{-1}$. Once boundary rotation is initiated, the system undergoes at least five full rotations before data are acquired. Images are acquired at a rate of two per second for up to 3 h.

Simulation details. Our Brownian dynamics simulations assume the particles interact via a Yukawa pair potential

$$V(r) = V_0 \frac{e^{-\kappa r}}{\kappa r}$$

with r denoting the inter-particle separation, κ the inverse Debye screening length, and V_0 the magnitude of the potential energy. In addition, each of the 27 particles in the outermost boundary layer is exposed to a harmonic potential mimicking the optical traps employed in experiment, given by

$$V_t(|\mathbf{r}_i - \mathbf{r}_{i,0}|) = \frac{k}{2}|\mathbf{r}_i - \mathbf{r}_{i,0}|^2$$

where $\mathbf{r}_i$ is the position of the ith particle and $\mathbf{r}_{i,0}$ is the centre of its potential well, with k denoting the trap strength. Each time step δt, the locations of the 27 harmonic potential minima, $\mathbf{r}_{i,0}$, are translated a predetermined arc length, l, along the boundary, resulting in a rotation velocity $l/\delta t$. The velocity, and thus Péclet number, is controlled by altering this arc length.

To account for the hydrodynamic effect of the planar substrate that is present in experiment we apply Blake's solution[37,38], which uses the method of images to obtain the Green's function of the Stokes equation satisfying the no-slip boundary condition at $z = 0$ as

$$G_{\alpha\beta}(\mathbf{r}_i, \mathbf{r}_j) = G^S_{\alpha\beta}(\mathbf{r}) - G^S_{\alpha\beta}(\mathbf{R}) + G^D_{\alpha\beta}(\mathbf{R}) - G^{SD}_{\alpha\beta}(\mathbf{R}) \quad (1)$$

where the indices i and j refer to spatial positions, with $\alpha, \beta = x, y, z$ being the coordinates. The vector $\mathbf{r}$ gives the relative position $\mathbf{r}_i - \mathbf{r}_j$, whereas $\mathbf{R} = \mathbf{r}_i - \mathbf{r}_j'$ denotes the relative position vector with the image of j at $\mathbf{r}_j' = (x_j, y_j, -z_j)$ with respect to the planar substrate at $z = 0$. Blake's solution in equation (1), relating the flow field at $\mathbf{r}_i$ to a unit point force at $\mathbf{r}_j$ in the presence of a boundary plane, comprises four contributions. First, the Green's function for the Stokeslet G^S (that is, if a unit point force is applied at the origin in an unbounded fluid)

$$G^S_{\alpha\beta}(\mathbf{r}) = \frac{1}{8\pi\eta}\left(\frac{\delta_{\alpha\beta}}{r} + \frac{r_\alpha r_\beta}{r^3}\right)$$

with $r = |\mathbf{r}|$, and η being the viscosity of the fluid. The second contribution is the image Stokeslet. The third is a Stokes doublet G^D

$$G^D_{\alpha\beta}(\mathbf{r}) = \frac{1}{8\pi\eta} 2z_j^2 (1 - 2\delta_{\beta z})\left(\frac{\delta_{\alpha\beta}}{r^3} - \frac{3r_\alpha r_\beta}{r^5}\right)$$

and the final term is a source doublet G^{SD}

$$G^{SD}_{\alpha\beta}(\mathbf{r}) = \frac{1}{8\pi\eta} 2z_j (1 - 2\delta_{\beta z})\left(\frac{\delta_{\alpha\beta} r_z}{r^3} - \frac{\delta_{\alpha z} r_\beta}{r^3} + \frac{\delta_{\beta z} r_\alpha}{r^3} - \frac{3r_\alpha r_\beta r_z}{r^5}\right)$$

By applying Blake's scheme to the 27 rotating particles located at $\mathbf{r}_j$, the αth component of the flow field reads

$$u_{\alpha=x,y}(\mathbf{r}_i) = \sum_{j=1}^{27} \sum_{\beta=x,y} G_{\alpha\beta}(\mathbf{r}_i, \mathbf{r}_j) f_\beta(\mathbf{r}_j) \quad (2)$$

where $\mathbf{f} = \gamma \dot{\mathbf{r}}_j$ is taken as the drag force applied at $\mathbf{r}_j$ caused by the rotation of the boundary, with γ being the Stokesian friction coefficient. Note that particle z-coordinates are fixed at $2z/\sigma = 1.03$, based on the gravitational length of the experimental colloids. Hence, we restrict our system to effectively two dimensions with vanishing force and flow components along the z-direction. The confined particles are further coupled to the flow field via the Stokes drag $\mathbf{F}_d(\mathbf{r}_i) = \gamma \mathbf{u}(\mathbf{r}_i)$, with $\mathbf{u}$ having components $u_{\alpha=x,y}$ as given in equation (2).

The equation for the trajectory $\mathbf{r}_i$ of particle i undergoing Brownian motion in a time step δt reads as

$$\mathbf{r}_i(t + \delta t) = \mathbf{r}_i(t) + \frac{D_0}{k_B T}\mathbf{F}_i(t)\delta t + \mathbf{u}(\mathbf{r}_i)\delta t + \delta \mathbf{W}_i$$

where $D_0 = k_B T/\gamma$ denotes the free diffusion constant, $k_B T$ the thermal energy, and $\mathbf{F}_i(t)$ is the total conservative force acting on particle i stemming from the pair interactions, V, and for the 27 driven wall particles also from the harmonic trap potential V_t. The third term on the right-hand side is the solvent flow field due to hydrodynamic effects, the details of which are given in equation (2). The random displacement $\delta \mathbf{W}_i$ is sampled from a Gaussian distribution with zero mean and variance $2D_0\delta t$ (for each Cartesian component) fixed by the fluctuation–dissipation relation.

We use the standard velocity Verlet integration to obtain the equation of motion for the particle trajectories, which contains the total conservative force acting on particles (stemming from the pair interactions and, for the 27 driven particles also from the harmonic trap potential), the random displacements (sampled from a Gaussian distribution obeying the fluctuation–dissipation relation) and the determined flow field. Colloid motion is coupled to the flow field via the Stokes drag.

The simulated unit length scale is set by κ, the energy scale by $k_B T$, and the timescale by $\tau_{sim} = 1/(\kappa^2 D_0)$. The inverse screening length κ is chosen as $\kappa\sigma = 30$, where the experimental value of σ serves as a reference. Consequently, the wall radius is $\kappa R_0 = 130$, yielding the experimental ratio of $R_0/\sigma = 4.33$. The high screening at $\kappa\sigma = 30$, together with the contact potential chosen as $V(r = \sigma) \approx 1.6 k_B T$, ensures the quasi hard-disc-behaviour. Another crucial parameter in our system is the trap strength, which has been set to $k = 0.42\kappa^2 k_B T$ to mimic the measured optical trap stiffness in the experiments. The time step is chosen as $\delta t = 10^{-4}\tau_{sim}$. Simulations run for up to $3 \times 10^4 \tau_{sim}$, corresponding to approximately $133.3\tau_B$, with τ_B being the experimental Brownian time.

Local structure. The degree of local hexagonal ordering is quantified using the bond-orientational order parameter, $\psi_6^j = |1/z_j \sum_{m=1}^{z_j} \exp(i6\theta_m^j)|$, where z_j is the coordination number as defined by a Voronoi construction and θ_m^j is the angle made by the bond between particle j and its mth neighbour and a reference axis. The curved boundary suppresses ψ_6^j in its vicinity. Thus we characterize the hexagonality of a configuration by averaging ψ_6^j over all confined particles that are non-adjacent to the boundary. Where ψ_6 is considered within particle layers, ψ_6^j is instead averaged over all particles in the layer in question.

Efficiency calculation. For completeness, here we provide a derivation of the isothermal efficiency. The total potential energy of the device is

$$U(\{\mathbf{r}_i\}, t) = \sum_{i=1}^{n} \frac{k}{2}|\mathbf{r}_i - \mathbf{r}_{i,0}(t)|^2 + U_0(\{\mathbf{r}_i\})$$

where the first contribution models the $n = 27$ optical traps through harmonic potentials with stiffness k and the second term accounts for the interaction energy of all particles. The potential energy is a function of all particle positions. It becomes explicitly time dependent as we manipulate the positions of the trap centres

$$\mathbf{r}_{i,0}(\varphi) = R\begin{pmatrix}\cos(2\pi i/n + \varphi)\\ \sin(2\pi i/n + \varphi)\end{pmatrix} \quad (3)$$

through changing φ (R is the distance of the traps from the origin). Although this is done stepwise in the experiments and simulations, for simplicity in the following we assume a constant angular velocity $\omega_{drive} = \dot{\varphi}$.

By moving the trap centres, the system is driven into a non-equilibrium steady state. The first law of thermodynamics dictates that the work spent to maintain this steady state is balanced by the dissipated heat and the change of internal energy (the signs are convention)[32],

$$đq = đw - dU$$

The symbol đ stresses the fact that work and heat are not exact differentials. Moreover, they are fluctuating quantities. The work is given by the energy change that is directly caused by the translation of the traps, $đw = \dot{w}dt$, with

$$\dot{w}(\{\mathbf{r}_i\}) = \partial_t U = \dot{\varphi}\sum_{i=1}^{n} f_i$$

and projected forces $f_i = -k(\mathbf{r}_i - \mathbf{r}_{i,0}) \cdot (\partial_\varphi \mathbf{r}_{i,0})$. Plugging in equation (3), the mean work rate becomes

$$\langle \dot{w} \rangle = n\,\omega_{\mathrm{drive}}\,R^2\,k\,\langle \sin\theta \rangle = n\,\omega_{\mathrm{drive}}\,\tau_{\mathrm{drive}} \geqslant 0$$

where $\theta_i = 2\pi i/n + \varphi - \varphi_i$ is the lag angle of the ith particle behind the trap centre. Clearly, its average is independent of the particle index; moreover, in equilibrium $\langle \theta \rangle = 0$ and therefore $\dot{w} = 0$. Note that the dynamics (and in particular hydrodynamic interactions) enter only through the average. We extract the lag angles and their average from both the experiments and simulations.

We identify $P_\mathrm{i} = \dot{w}$ with the input power. Applying a load torque τ, the extracted power reads $P_\mathrm{o} = \tau\omega$, where $\omega(\tau)$ is the (load-dependent) angular velocity of the axle. The isothermal efficiency finally is defined as the ratio[3]

$$\eta = \frac{P_\mathrm{o}}{P_\mathrm{i}} = \frac{1}{n}\,\frac{\omega}{\omega_{\mathrm{drive}}}\,\frac{\tau}{\tau_{\mathrm{drive}}}$$

of output to input power.

References

36. Crocker, J. C. & Grier, D. G. Methods of digital video microscopy for colloidal studies. *J. Colloid Interface Sci.* **179,** 298–310 (1996).
37. von Hansen, Y., Hinczewski, M. & Netz, R. R. Hydrodynamic screening near planar boundaries: Effects on semiflexible polymer dynamics. *J. Chem. Phys.* **134,** 235102 (2011).
38. Blake, J. R. A note on the image system for a Stokeslet in a no-slip boundary. *Proc. Camb. Phil. Soc.* **70,** 303–310 (1971).